

ORIGINAL RESEARCH

Open Access



Potentials of emergent plant residue derived biochar to be alternative carbon-based phosphorus fertilizer by Fe(II)/Fe(III) magnetic modification

Hongjuan Xin¹, Jiao Yang¹, Yuanyuan Lu¹, Hekang Xiao¹, Haitao Wang¹, Kamel M. Eltohamy^{1,2}, Xueqi Zhu³, Chunlong Liu³, Yunying Fang⁴, Ye Ye^{5*} and Xinqiang Liang^{1,3*}

Abstract

Emergent plants have been remarkably effective in reducing phosphorus (P) discharge from ecological ditches; however, the treatment and recycling of these residues is a great challenge. In this study, magnetic biochars (MB_s, i.e., MB-A, MB-C, and MB-T) were fabricated from three emergent plant residues (*Acorus calamus* L., *Canna indica* L., and *Thalia dealbata* Fraser, respectively) and modified with Fe(II)/Fe(III). Scanning electron microscopy-energy dispersive spectroscopy and X-ray diffraction spectra confirmed the successful loading of Fe₃O₄ and FeO(OH) onto the surfaces of the MB_s. Batch adsorption experiments showed that MB_s exhibited a higher P adsorption capacity than that of the raw biochars. Within the range of 0.8–43.0 mg L⁻¹ in solution, the adsorption capacities of P by MB-A, MB-C, and MB-T were 304.6–5658.8, 314.9–6845.6, and 292.8–5590.0 mg kg⁻¹, with adsorption efficiencies of 95.2–32.9%, 98.4–39.8%, and 91.5–32.5%, respectively. The primary mechanisms that caused P to adsorb onto the MB_s were inner-sphere complexation and electrostatic attraction. Low pH conditions were more beneficial for the P adsorption of the MB_s, while co-existing anions had a negative impact with the following order: HCO₃⁻ > SO₄²⁻ > Cl⁻ ≈ NO₃⁻. The P-31 nuclear magnetic resonance results further demonstrated that the main adsorbed P species on the MB_s was orthophosphate, followed by orthophosphate monoesters and DNA. Overall, MB_s offer a resource utilization strategy for emergent plant residues and P-laden MB_s are promising alternative P fertilizers.

Highlights

- Emergent plant biochar modified with Fe(II)/Fe(III) enhanced P adsorption capacity.
- *Canna indica* residue-derived MB exhibited the best P adsorption efficiency.
- MB_s promoted P adsorption mainly via inner-sphere complexation and electrostatic attraction.
- P species adsorbed by MB_s were mainly orthophosphate followed by orthophosphate monoesters and DNA.

Handling editor: Xiangzhou Yuan.

*Correspondence:

Ye Ye

ye200506@163.com

Xinqiang Liang

liang410@zju.edu.cn

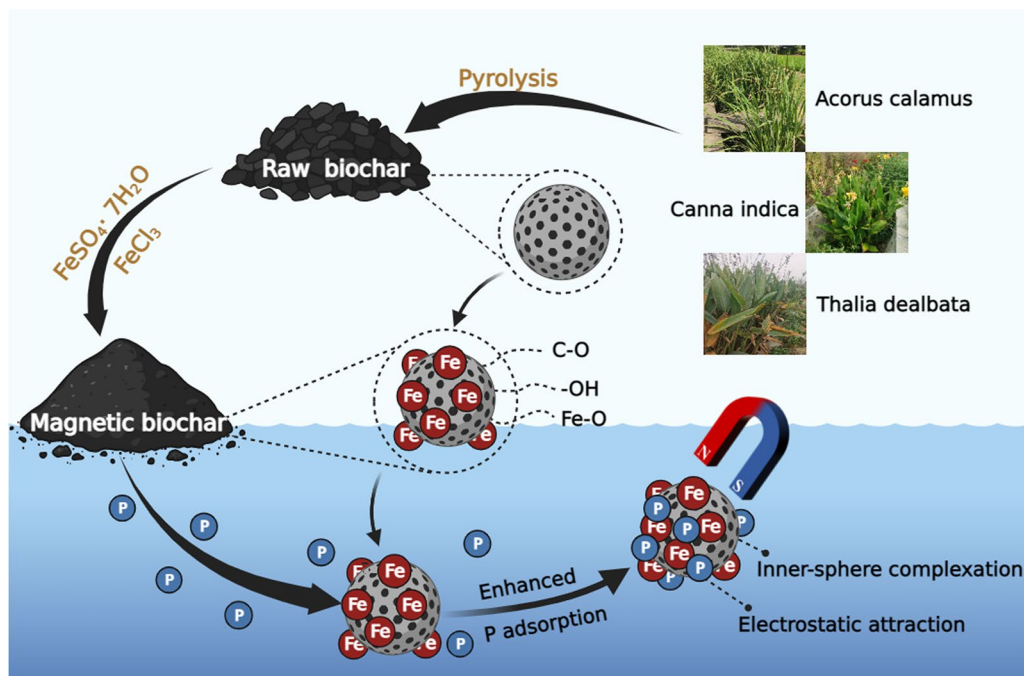
Full list of author information is available at the end of the article



© The Author(s) 2024. **Open Access** This article is licensed under a Creative Commons Attribution 4.0 International License, which permits use, sharing, adaptation, distribution and reproduction in any medium or format, as long as you give appropriate credit to the original author(s) and the source, provide a link to the Creative Commons licence, and indicate if changes were made. The images or other third party material in this article are included in the article's Creative Commons licence, unless indicated otherwise in a credit line to the material. If material is not included in the article's Creative Commons licence and your intended use is not permitted by statutory regulation or exceeds the permitted use, you will need to obtain permission directly from the copyright holder. To view a copy of this licence, visit <http://creativecommons.org/licenses/by/4.0/>.

Keywords Emergent plant, Fe(II)/Fe(III) modification, Magnetic biochar, Phosphorus adsorption, Phosphorus species

Graphical Abstract



1 Introduction

Phosphorus (P) is a nonrenewable resource, and it is predicted that global P reserves will be depleted within 100 years if no solution is taken (Smit et al. 2009). Since P is essential for plant growth, large amounts of P continuously enter the environment with the development of agriculture, causing the wastage of P resources and water eutrophication (Conley et al. 2009). Recently, several countries have implemented strict thresholds for P concentrations in the environment. Total phosphorus (TP) emissions should not exceed 1 mg L^{-1} in class 1B and 0.5 mg L^{-1} in class 1A (MEP 2002). The US EPA advised that TP levels in streams entering lakes should be below $50 \mu\text{g of P L}^{-1}$ (Loganathan et al. 2014). In response to the upgrading of emission standards, the development of more effective measures to mitigate P pollution and promote P recycling is urgently required.

Ecological ditches are one of the most effective methods for mitigating agricultural P pollution by virtue of their ability to remove P (Kröger and Moore 2011; Kumwimba et al. 2017). Emergent plants, in particular, are frequently utilized in environmental remediation because

of their high P uptake, low cost, and visual attractiveness (Singh et al. 2023). Emergent plants can adsorb P directly and store it in their biomass. The P uptake rates of emergent plants have been reported to be $1\text{--}4 \text{ kg of dry matter m}^{-2} \text{ yr}^{-1}$ or more (Iamchaturapatr et al. 2007; Christopher 2013; Wu et al. 2023). However, many emergent plants wilt and rot during winter, which poses a risk of secondary water contamination; thus, they must be harvested regularly (Yu et al. 2019). Current methods for treating emergent plants mainly include composting and incineration; however, these methods suffer from inefficiencies and long processing times (Gusain et al. 2018). Therefore, the next crucial step is to create efficient and eco-friendly alternative utilization strategies for emerging plant residues.

Biochar is expected to be a reliable P-adsorption material because of its cost-effectiveness and unique properties that can be easily obtained by biomass pyrolysis in an anaerobic or oxygen-limited environment (Klinar 2016). With in-depth research into engineered biochar, the feedstock options for raw biochar are continuously increasing (Cheng et al. 2023), however, these were found

to have a limited P adsorption ability because of the negative charge on their surface (Shepherd et al. 2017; Liu et al. 2022). To overcome this problem, metal-modified biochars have received increasing attention owing to their strong affinity for P (Palansooriya et al. 2021; Padilla et al. 2023). Currently, metals including iron (Fe), calcium (Ca), and magnesium (Mg) are frequently utilized to modify biochar because of their low cost and lack of secondary pollution (Jiang et al. 2018; Mitrogiannis et al. 2018; Chen et al. 2022). In addition, Fe-based biochars have the advantage of magnetic recovery, offering the ability to separate these from solution (Huang et al. 2019; Palansooriya et al. 2021). According to previous studies, Fe-modified biochar can increase the surface positive charge, thereby improving the anion exchange capacity and redox properties of the biochar (Ou et al. 2023). Wang et al. (2020a, b)'s study validated that Fe-modified biochar had a greater adsorption capacity (1.84 mg g^{-1}) for P than raw biochar (no effect) and Palansooriya et al. (2021) also found comparable outcomes in their study of Fe(III)-loaded chitosan biochar. Mixed metal oxides/hydroxides containing multiple metal components possess the benefits of parent metals and produce synergies that improve their adsorption properties (Wu et al. 2020). Although reports are available on the effect of Fe-modified materials since over two years ago, little attention has been paid to Fe(II) and Fe(III) modification of biochars for P adsorption.

Additionally, after P adsorption, biochar has the potential to be functionalized as a P fertilizer. Ai et al. (2023) used corn stalk biochar after P adsorption as a fertilizer and observed that it significantly promoted plant growth. Nevertheless, the variation in the bioavailability of the P species adsorbed by biochar in actual water is not clear because most studies tested the performance of biochar as a P adsorbent in phosphate solutions. In this study, to reduce P discharge into external water bodies and to reuse plant residues, we prepared Fe(II)/Fe(III) co-modified biochars using three types of emergent plant residues for application in P adsorption from wastewater. The aims of this study were: (i) to investigate the P adsorption capacity of biochars derived from emergent plant residues, (ii) to explore the P adsorption processes and mechanisms of magnetic biochars (MB_s), and (iii) to identify the P species in P-laden biochars and provide data for the effective support of using these as P fertilizers. The results of this study offer an efficient adsorbent for P adsorption and a greater understanding of the P species adsorbed by MB_s, which will be helpful for the further utilization of MB_s in P adsorption, fertilizer, and resource cycling engineering.

2 Materials and methods

2.1 Preparation of RBs

Three emergent plants (*Acorus calamus* L., *Canna indica* L., and *Thalia dealbata* Fraser) were collected from ecological ditches in Pinghu County, Zhejiang Province, China. Emergent plant residues were cleaned with deionized (DI) water before use, dried in an oven for 2 h at 105°C, and further dried at 60°C. The dried residue was cut into fragments smaller than 5 cm, crushed, and filtered through a 0.15 mm pore size filter. The treated residue was pyrolyzed in a programmable electric tube furnace (OTF-1200X, Hefei kejing materials technology Co., Ltd, China). The system temperature was raised to 650 °C at a pace of 10 °C min⁻¹ and the high temperature was maintained for 0.5 h under N₂ conditions (Zhao et al. 2022). The yields of the three biochars were approximately 29%. These raw biochars (RBs) were denoted as RB-A, RB-C, and RB-T and were produced from the residues of *Acorus calamus* L., *Canna indica* L., and *Thalia dealbata* Fraser, respectively.

2.2 Preparation of MB_s

The MB_s were prepared as follows: 2.5 g of each RB was placed into 50 mL of mixed iron (Fe) solution (0.01 mol FeSO₄·7H₂O and 0.01 mol FeCl₃), heated at 60°C for 30 min under slow stirring, cooled to 40°C, and then 5 M NaOH was added to maintain the pH at 10–11 (Dai et al. 2020). The mixture was stirred for 10 min and aged for 24 h. The black precipitate was collected and cleaned with DI water and ethanol. The MB_s were finally obtained after filtration and drying at 60°C for 24 h. Modified RB-A, RB-C, and RB-T were named MB-A, MB-C, and MB-T, respectively. By dispersing the MB_s evenly in pure water, aggregation of the suspended powder was observed under the attraction of magnets. Thus, the MB_s were confirmed to be highly magnetic and could be successfully separated from water via magnetic separation (Additional file 1: Fig S1).

2.3 Adsorption experiments

The P adsorption ability of the MB_s was assessed using batch adsorption tests. All the solutions used for the adsorption experiments were obtained from a livestock breeding farm in Kaihua, Zhejiang Province, China. The experiments were conducted at 120 rpm and 25 °C for 24 h. To evaluate the adsorption capacity of the RBs, 100 mg of RBs were added to 40 mL of the diluted solution. Similarly, 100 mg of RBs were added to 40 mL of solution with the initial P concentration in the range from 0.8 mg L⁻¹ to 43 mg L⁻¹ to examine the adsorption abilities of the RBs. The adsorption kinetic tests were completed

at 25 °C with the TP concentration of the solution at 20 mg L⁻¹. Samples were periodically collected at a mixture time after 2, 4, 6, 8, 10, 20, 30, 60, 90, 180, 360, 720, and 1440 min. The P content of the solution was analyzed using the molybdenum blue colorimetric method (Lei et al. 2021). The experimental data were fitted with pseudo-first-order, pseudo-second-order, and intra-particle diffusion models to understand the adsorption kinetics.

The influence of the solution pH on adsorption was investigated by conducting experiments at pH levels between 3 and 11. The pH of the solution was adjusted using 0.2 M HCl or NaOH solutions. The method of pH drift was used to quantify the point of zero charge (pH_{PZC}) of the adsorbent (Villanueva et al. 2014). In addition, possible interferences between co-existing anions (sulfate (SO₄²⁻), chlorine (Cl⁻), nitrate (NO₃⁻), and bicarbonate (HCO₃⁻) and P adsorption by MB_s were investigated. Different co-existing anions of the same concentration (1 M) were added to the solution under the same conditions, including pH. The P adsorption experiment followed the same procedure, with 100 mg of MB_s added to 40 mL of solution and oscillated for 24 h at 120 rpm and 25 °C.

In the above experiments, the amount of P in the solution was determined using a UV-vis spectrometer (UV-9000, Shanghai Metash Instruments Co., Ltd., China) following the molybdate blue spectrophotometric method. The pH of each solution was measured using an HQ 11D pH meter (HACH, USA). The average values for each experiment were obtained from three replicates.

2.4 Characterization of biochars

Microscopic features and morphology of the biochars were characterized using scanning electron microscopy-energy dispersive spectroscopy (SEM-EDS; Gemini SEM-EDS 300; ZEISS, Germany). The crystal structures of the MB_s were analyzed by X-ray diffraction (XRD; Bruker D8 Advance, Germany). The surface functional groups of the RMs and MB_s were examined by Fourier transform infrared spectroscopy (FTIR, Nicolet is50 FTIR, Thermo Scientific, USA) with a wavenumber range of 400–4000 cm⁻¹. X-ray photoelectron spectroscopy (XPS, Thermo Scientific Escalab 250xi, USA) was used to analyze the elemental states on RMs before and after adsorption.

2.5 Phosphorus species of the MB_s before and after adsorption

The P species were determined using a slightly altered version of the Cade-Menun and Preston (1996)

approaches. Specifically, P on the MB_s before and after adsorption was extracted and examined using solution P-31 nuclear magnetic resonance (³¹P-NMR) spectroscopy. First, 2.0 g of samples and 40 mL of NaOH-Na₂EDTA mixture solution (0.25 M NaOH and 0.05 M Na₂EDTA) were put in centrifuge tubes, shaken gently at 20 °C for 16 h, then centrifuged at 5000 rpm for 20 min. One milliliter of the supernatant was used for inductively coupled plasma optical emission spectroscopy (ICP-OES) analysis. Freeze-dried samples were dissolved in 0.65 mL of deuterium oxide (including 0.84 mg mL⁻¹ methylenediphosphonic acid (MDPA)), 0.65 mL of distilled water, 0.4 mL of 10 M NaOH, and 0.65 mL of NaOH-EDTA solution. The dissolved samples were vortexed for 10 min and centrifuged at 5000 rpm for 20 min, then 0.7 mL was transferred into 5-mm NMR tubes. The NMR parameters included 90° pulse, 0.68-s acquisition time, 4.0-s pulse delay, 10 Hz spinning, 20 °C, and 2400–2800 scans for different samples depending on the P concentration. The quantities of various P species were analyzed by calculating the relative integral of the peak area versus MDPA using MestReNova (version 7.0, Mestrelab Research, Spain). The position of orthophosphate was adjusted at 6.0 ppm, the peaks between 5.0 and 4.3 ppm were sequentially determined as orthophosphate monoesters, the peak around -0.7 ppm was determined as DNA, and the peaks from -4.0 to -4.2 ppm were determined as pyrophosphate (Liu et al. 2018).

2.6 Phosphorus release tests

The P release capability of the MB_s after P adsorption (P-laden MB_s) was measured using DI water as the release medium. The specific steps were as follows: 100 mg of P-laden MB_s was added to 40 mL of DI water, and the mixture was shaken at 25 °C and 120 rpm for sampling at 1, 2, 3, 6, 10, 24, 48, 72, 120, 144, 168, and 192 h. The results were fitted to second-order release kinetics. The P-laden MB_s were reintroduced into distilled water for cyclic P release at 72 h. The P content was determined using molybdate blue spectrophotometry. The P release experiments were conducted three times, and the average and standard deviation were calculated.

2.7 Statistical analysis

Data were analyzed using SPSS (version 26.0, IBM, USA) and the results were visualized using Origin 2021 (Origin Lab, USA). Significant differences in the P adsorption content were tested using a one-way analysis of variance (ANOVA) with the least significant difference (LSD) test at the 5% level ($p < 0.05$).

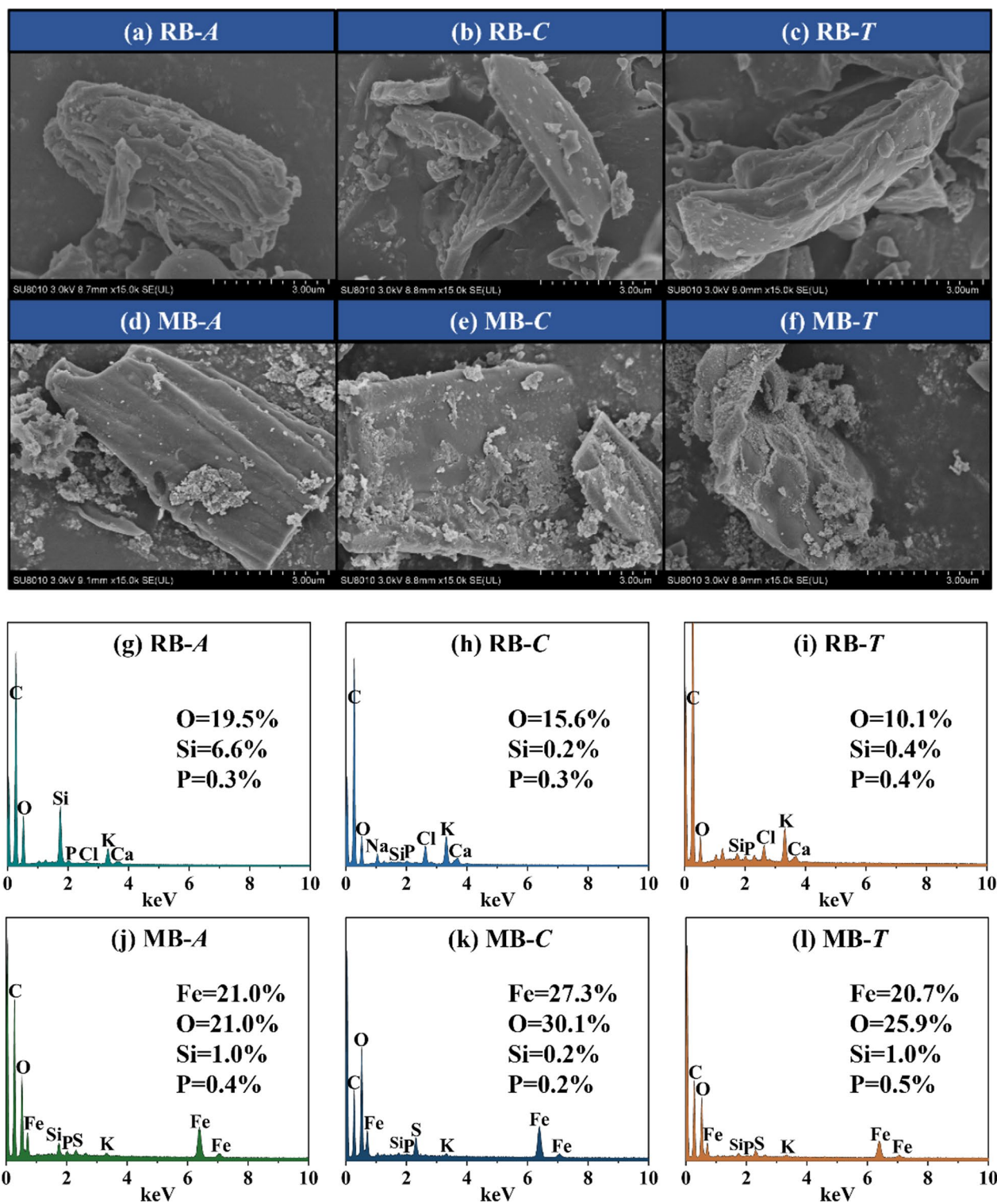


Fig. 1 SEM images (a–f) and EDS spectra (g–l) of RBs and MBs

3 Results and discussion

3.1 Characteristics of biochars

SEM was used to observe the microstructures of RBs and MB_s (Fig. 1). As shown in Fig. 1a–c, the surface morphology of the RBs appeared smooth and irregular, whereas the MB_s exhibited disordered particles on the surface (Fig. 1d–f). The EDS results (Fig. 1j–l) confirmed that the Fe content in the MB_s exceeded 20%, indicating that Fe-related complexes were successfully loaded onto the MB_s surface. Simultaneously, the disordered particles on the MB_s were iron oxides, which provide binding sites for P adsorption. Notably, the Fe content in MB-C reached 27.3%, indicating its potential for a higher adsorption capacity than that of the other MB_s (Huang et al. 2021).

The XRD patterns of the RBs and MB_s revealed six peaks corresponding to crystalline substances (synthetic minerals) (Fig. 2a). The RBs were mainly composed of potassium chloride (KCl) and calcite (CaCO₃), whereas the MB_s contained magnetite (Fe₃O₄) and goethite (FeO(OH)). These results show that Fe modification changed the predominant mineral composition of biochars, with the major substance changing from KCl or CaCO₃ to Fe₃O₄ or FeO(OH). The transformation of Fe(III) into FeO(OH) and Fe₃O₄ was consistent with the previous report of: FeCl₃ → Fe(OH)₃ → FeO(OH) → Fe₃O₄ (Li et al. 2016). Fe(III) loaded onto biochar reacted directly with P to form precipitates, whereas FeO(OH) interacts with P to produce complexes (Yang et al. 2018; Min et al. 2020). Furthermore, Fe(II) also contributed to the doping of Fe₃O₄ on biochars, enhancing the magnetic separation and adsorption capabilities of the biochar (Reguyal et al. 2017; Zhou et al. 2017; Dong et al.

2018). The Fe oxide layer on the MB_s surface was the primary reason for the enhanced P adsorption.

3.2 Phosphorus adsorption capacities and mechanism of biochars

The capability of RBs for P adsorption was investigated using a 2.5 mg L⁻¹ P solution, however, it demonstrated a desorption phenomenon of P from raw materials (Fig. 3a), possibly owing to the negative surface charge on RBs, which was not conducive to P adsorption (Ahmad et al. 2014). Therefore, RBs were excluded from the subsequent P adsorption studies. The P-adsorption performance of the MB_s is shown in Fig. 3b. At 0.8 mg L⁻¹ (low concentration of P), the adsorption efficiency of all MB_s was above 90%. As the solution's P content increased from 0.8 to 43.0 mg L⁻¹, the P adsorption efficiency decreased owing to the limited availability of adsorption sites. However, at the initial concentration of 22.0 mg L⁻¹, the adsorption efficiency of MB-A, MB-C, and MB-T was still 61.7%, 76.0%, and 57.2%, respectively. The results showed that the MB_s had a stronger P-adsorption capacity than the RBs, and that MB-C was the most efficient among the three MB_s.

To enhance our comprehension about the P adsorption process onto MB_s, adsorption studies were conducted with varying contact times. Kinetic models play a significant role in elucidating the pathways and mechanisms associated with adsorption processes (Gong et al. 2019). As depicted in Fig. 3c, the P adsorption of all MB_s was rapid during the first two hours before slowing down and reaching equilibrium at approximately 6 h. The initial rapid adsorption can be attributed to the large number of binding sites and the electrostatic attraction between the phosphates and positively charged Fe or Fe oxides

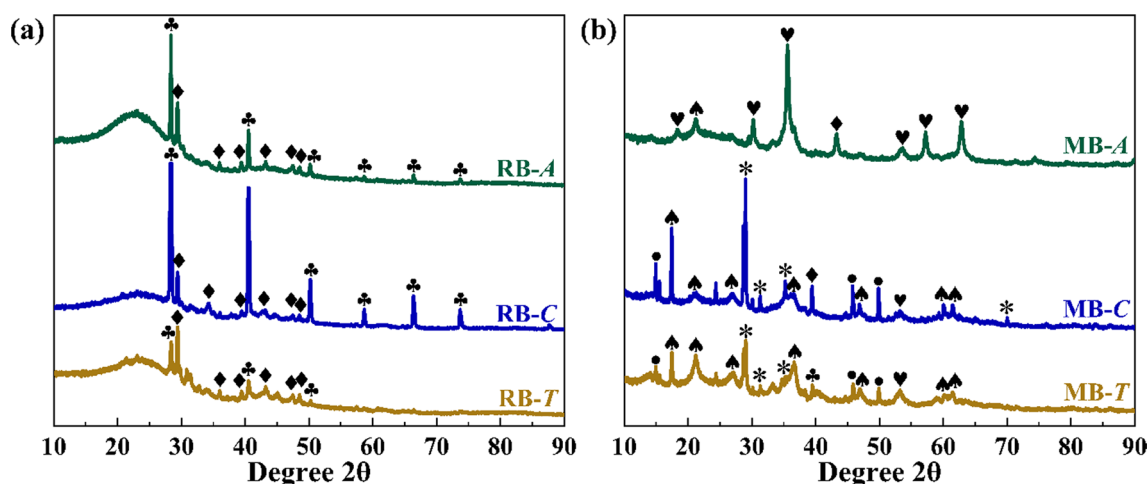


Fig. 2 The XRD spectra of RBs and MB_s. Notes: ♠ Sylvite-KCl; ◆ Calcite-CaCO₃; ♥ Magnetite-Fe₃O₄; ♣ Goethite-FeO(OH); • Chloromagnesite-MgCl₂; * Magnesium Chlorate-Mg(H₂O)₆(ClO₂)₂

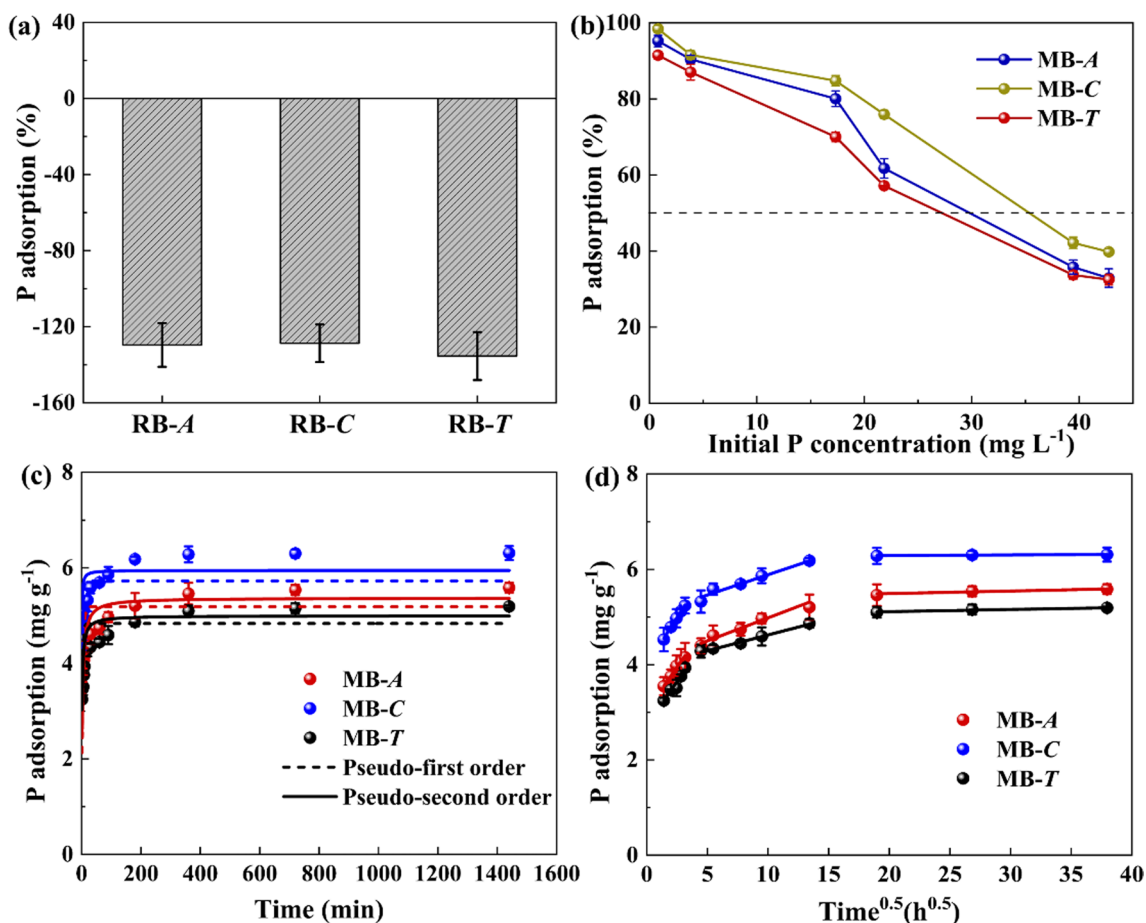


Fig. 3 P adsorption performance of RBs (a) and MBs (b); adsorption kinetics of MBs fitting by Pseudo-first-order and Pseudo-second-order model (c); adsorption kinetics of MBs fitting by intraparticle diffusion model (d)

(Shan et al. 2021). Notably, this behavior was consistent across different types MBs. The adsorption parameters for the pseudo-first-order and pseudo-second-order models are listed in Table 1. Among all MBs, the pseudo-second-order model exhibited a better fit ($R^2 \geq 0.87$) than the pseudo-first-order model ($R^2 \geq 0.63$), indicating that chemical adsorption was the rate-determining step (Yi et al. 2019).

The experimental data were fitted using an intra-particle diffusion model to enhance our understanding of the rate-limiting steps. This model was used to explain the diffusion of P onto the adsorbent particle pores (Tran et al. 2017). The P adsorption process was divided into three sections (Fig. 3d), and the related parameters are listed in Table 1. The results revealed that the slope of the first stage was the highest of the three stages, implying a gradual decrease in the reaction rate with increasing contact time (Malash and El-Khaiary 2010). The rapid adsorption stage was caused by an external mass transfer phase, which may have been influenced by the

high density of P-binding sites on the surface of the MBs (Fang et al. 2022). Subsequently, the rate of P adsorption decreased, and P began to diffuse within the solid biochar particles, which is known as an intra-particle diffusion process (Yu et al. 2021). The third stage of adsorption reached equilibrium when no accessible adsorption sites were present on the MBs (Yao et al. 2013). Additionally, the first lines did not pass through the origin, indicating that intra-particle diffusion was not the sole rate-limiting process (Li et al. 2019).

The functional groups of RBs, MBs and P-laden MBs were examined by FTIR (Fig. 4b–d). Wide absorption bands approximately 3390 cm^{-1} were observed in MBs samples and were linked to the stretching vibrations of $-\text{OH}$, which were vibrationally enhanced with the addition of Fe (Yin et al. 2018). The 1630 cm^{-1} peak corresponded to the stretching vibration of $-\text{OH}$, arising from the distortion and movement of adsorbed water molecules (Ajmal et al. 2018). The peak at approximately 1085 cm^{-1} was associated with the deformation

Table 1 The parameters of kinetic and intra-particle diffusion models about P adsorption onto MB_s

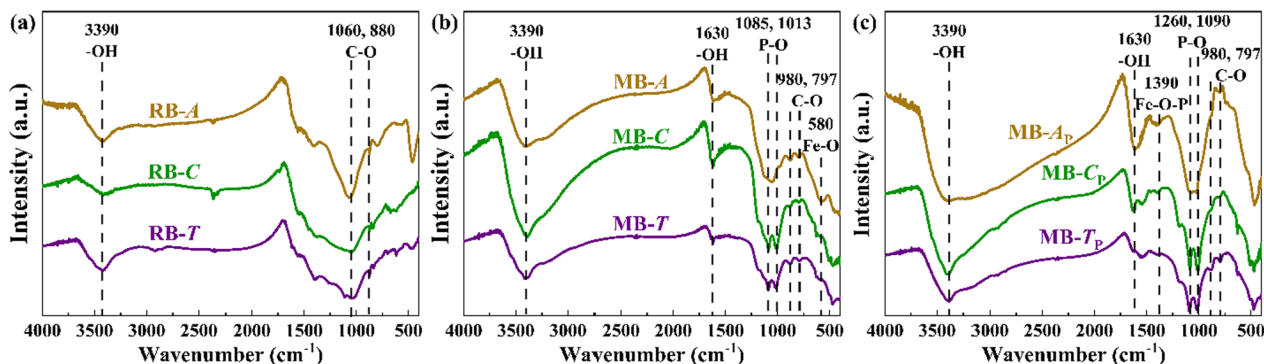
Models	Parameters	MB-A	MB-C	MB-T
Kinetic models				
Pseudo-first order	$q_{e(1)}$	5.19	5.76	4.84
	k_1	0.26	0.44	0.39
	R^2	0.73	0.88	0.63
Pseudo-second order	$q_{e(1)}$	5.37	5.84	4.99
	k_1	0.08	0.19	0.15
	R^2	0.91	0.94	0.87
Intra-particle diffusion models				
First stage	a	0.366	0.400	0.365
	b	3.033	3.990	2.734
	R^2	0.98	0.99	0.99
Second stage	a	0.097	0.086	0.066
	b	4.015	5.037	3.962
	R^2	0.96	0.98	0.99
Third stage	a	0.005	0.001	0.004
	b	5.386	6.259	5.024
	R^2	0.91	0.93	0.98

The parameters " q_e " and " k_1 " represent the equilibrium adsorption capacity and kinetic constant calculated by the model, respectively. And " a " and " b " represent the fitted slope and y-axis intercept, respectively

vibration of P–O in iron phosphates, providing evidence for the presence of phosphate in the MB_s (Zhang et al. 2019). After adsorption, these peaks became more pronounced, indicating successful adsorption of P onto the MB_s surface. The characteristic vibration of C–O bonds was attributed to the peaks observed at 980 cm⁻¹ and 797 cm⁻¹ (Zhao et al. 2022). These two peaks weakened after P adsorption, suggesting that phosphate entered the exchange layer and was exchanged (Jiang et al. 2020). The peak at 580 cm⁻¹ was attributed to the Fe–O stretch vibration of magnetite and it disappeared after P adsorption, which might be attributed to the strong adsorption of phosphate on the metal oxide surface (Wang et al.

2023). A novel peak at 1390 cm⁻¹ was related to the stretching vibration of Fe–O–P, which belonged to inner-sphere surface complex (Wang et al. 2021a, b). P adsorption onto MB_s was controlled by the inner-sphere surface complex formation process while maintaining structural and chemical stability.

Figure 5 shows that the P 2p peak intensity of MB_s was stronger after P adsorption, demonstrating that P was adsorbed on the MB_s surface. The high-resolution P 2p spectrum (Fig. 5b) showed a clear separation, revealing two individual peaks (2p1/2 and 2p3/2). Novel bonds were created by P adsorption. The primary component at binding energy (BE)=133.0–133.4 eV was pentavalent tetra coordinated P (PO₄³⁻) and the peak around 134.0 eV was attributed to HPO₄²⁻ (Xie et al. 2014). Moreover, the BE of the P 2p peaks of the three MB_s differed, with MB-C_p (P-laden MB-C) having the highest BE, indicating that it exhibited the strongest P binding (Gao et al. 2019). Additionally, Fe peaks were clearly visible in the XPS survey of the MB_s, indicating that Fe was successfully loaded onto the MB_s (Fig. 5c, d). The two peaks visible in the Fe 2p spectra were Fe 2p3/2 and Fe 2p1/2, with the former being narrower and stronger than the latter (Yamashita and Hayes 2008). The 711.4 eV and 713.8 eV of the Fe 2p3/2 spectra were associated with Fe(II) and Fe(III), respectively (Tang et al. 2023). The satellite peaks observed at approximately 719.0 eV and 732.0 eV were attributed to Fe 2p3/2 and Fe 2p1/2 respectively, confirming the Fe loaded on the MB_s existed in the form of γ -Fe₂O₃ (Hao et al. 2018; Tu et al. 2020). After P adsorption, the peak position of Fe 2p remained similar, indicating that Fe maintained its oxidation state during the adsorption process (Yang et al. 2022). The binding energies of the main peaks were consistent with the slightly shifted satellite peaks. These phenomena revealed that the MB_s adsorbed P by relying on active Fe sites.

**Fig. 4** The FTIR spectra of RBs (a), MB_s (b), and P-laden MB_s (c)

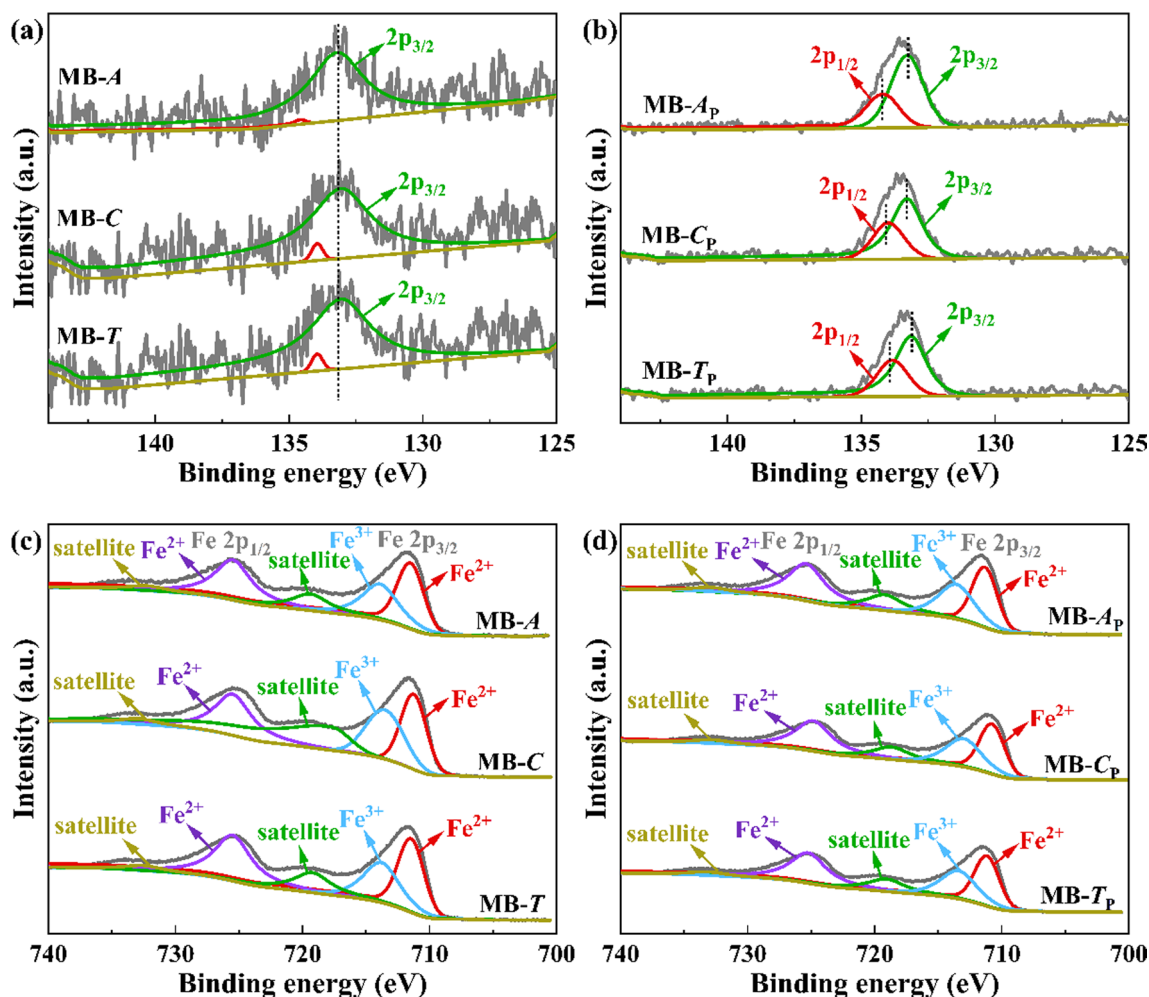
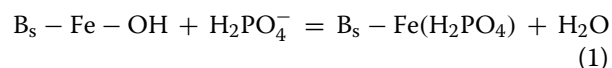


Fig. 5 XPS spectra of MB_s (a, c) and P-laden MB_s (b, d)

pH is a key influencing factor that affects the charge on the adsorbent's surface and the dissociation equilibrium of phosphate; therefore, the effect of starting pH levels on P adsorption by MB_s and the equilibrium pH of the solution after P adsorption were explored (Fig. 6a–c). Moreover, we found that the pH_{PZC} values of MB-A, MB-C and MB-T were 3.85, 3.33, and 3.28, respectively (Fig. 6d). As the initial pH rose from 3 to 11, the P adsorption capacity of MB-A, MB-C, and MB-T decreased from 7.8 to 5.5 mg g^{-1} , 7.9 to 5.2 mg kg^{-1} , and 6.4 to 5.4 mg g^{-1} , respectively. When the solution pH fell below the pH_{PZC} , a strong electrostatic attraction developed between the binding sites on the MB_s and H_2PO_4^- ions, increasing P adsorption (Hartley et al. 1997). As the pH increased, the charge on the surface of the adsorbent shifted in the negative direction and formed a repulsive charge with the phosphates, causing the P adsorption capacity to decline (Liu et al. 2021). Additionally, the solution pH

increased after P adsorption, which could be attributed to the complexation processes between P and the hydroxyl groups on the MB_s, which consisted of the formation of inner-sphere surface complexes (Xu et al. 2019). In the preliminary stage, electrostatic attraction occurred between the negatively charged phosphates and the electropositive MB_s surfaces loaded with amorphous hematite with a high zeta potential. During the subsequent adsorption process, inner-sphere complexation through ligand exchange played a significant role between the surface-bound Fe oxides/hydroxyl groups and phosphates (representative equilibrium; Eq. (1) is given below, taking H_2PO_4^- as an example).



As shown in Table 2, the P adsorption capacity was negatively affected by the ions SO_4^{2-} , Cl^- , NO_3^- , and

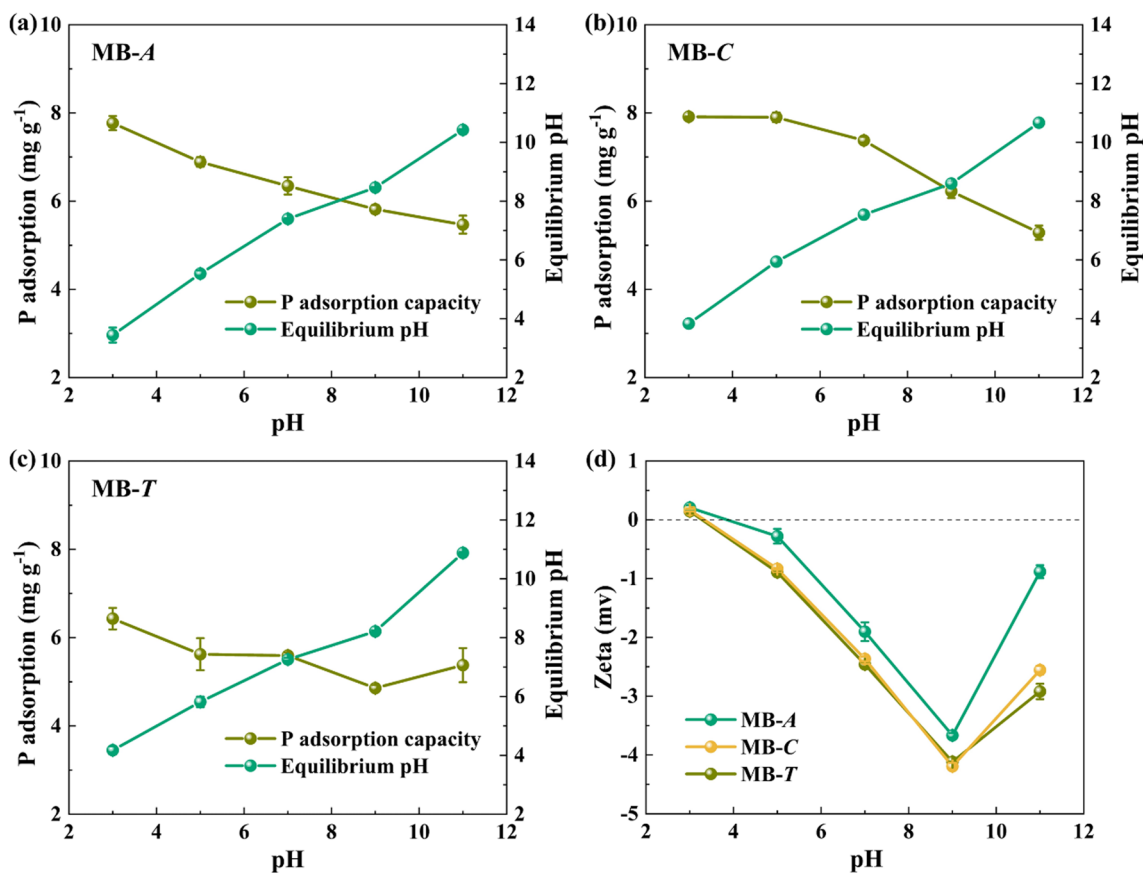


Fig. 6 Effects of pH on P adsorption capacity and equilibrium pH of MB-A (a), MB-C (b), MB-T (c); Zeta potential of MB_s (d)

Table 2 The effects of co-anions about P adsorption onto MB_s

Treatments	P adsorption (mg g ⁻¹)		
	MB-A	MB-C	MB-T
Control	5.58 ± 0.02 ^{Ba}	6.60 ± 0.10 ^{Aa}	5.23 ± 0.12 ^{Ca}
Cl ⁻	5.06 ± 0.14 ^{Bb}	6.37 ± 0.11 ^{Ab}	4.68 ± 0.10 ^{Cb}
NO ₃ ⁻	5.08 ± 0.11 ^{Bb}	6.38 ± 0.04 ^{Ab}	4.73 ± 0.10 ^{Cb}
SO ₄ ²⁻	4.51 ± 0.03 ^{Bc}	5.96 ± 0.01 ^{Ac}	4.20 ± 0.02 ^{Bc}
HCO ₃ ⁻	3.89 ± 0.24 ^{Bd}	5.84 ± 0.10 ^{Ac}	3.82 ± 0.11 ^{Bd}

Capitalized letters and lowercase letters represent significant differences in MB_s and anions at $p < 0.05$, respectively

HCO₃⁻. Of these, HCO₃⁻ imposed the most significant effect on the P adsorption capacity, decreasing it by 30.3%, 11.5%, and 27.0% for MB-A, MB-C, and MB-T, respectively. Because HCO₃⁻ had a higher distribution coefficient, causing significant interference to phosphate adsorption (Pitakteeratham et al. 2013). Another non-negligible negative effect was from SO₄²⁻ on P adsorption with obvious reduction rates of 19.1%, 9.7%, and 19.7% for MB-A, MB-C, and MB-T, respectively. This may be owing to SO₄²⁻ competing for complexation reaction

Table 3 P species of MB_s before and after P adsorption

Treatments	Orthophosphate (mg P g ⁻¹)	Orthophosphate monoesters	DNA	Pyrophosphate
MB-A	0.30	–	–	0.02
MB-C	1.37	–	–	–
MB-T	0.53	–	–	–
MB-A _p	7.99	0.04	0.03	0.03
MB-C _p	9.44	0.35	0.06	0.01
MB-T _p	7.99	0.04	0.06	0.01

“–” represents that the information is not available

sites with phosphate (Drenkova-Tuhtan et al. 2013). Conversely, Cl⁻ and NO₃⁻ were related to outer sphere compounds forming (Wang et al. 2020a, b). They showed a slight adverse impact on P adsorption, indicating that the affinity for Cl⁻ and NO₃⁻ was relatively low and inner-sphere adsorption plays a primary role in P adsorption (Fang et al. 2022). MB-C adsorbed more P than MB-A and MB-T for the different co-existing anions, validating that MB-C had the strongest P adsorption ability.

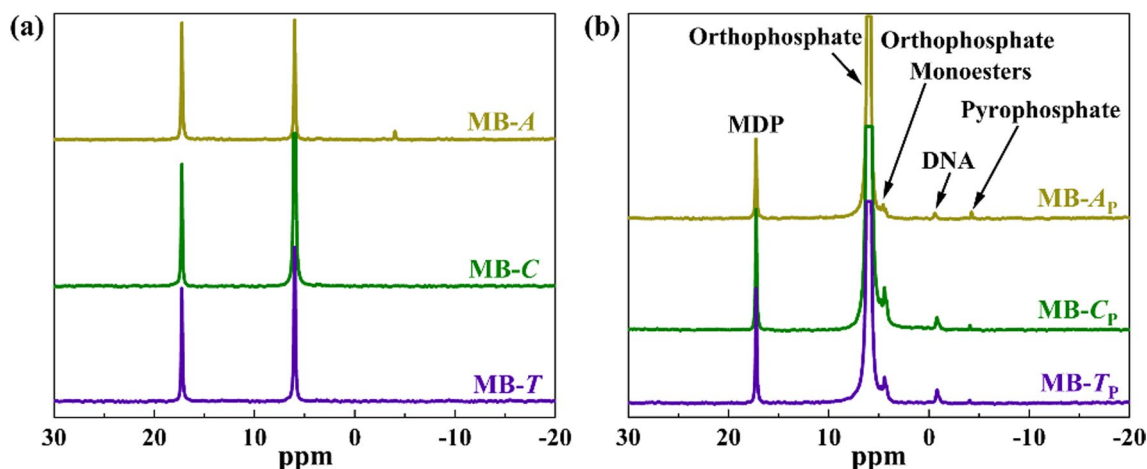


Fig. 7. ^{31}P -NMR spectra of MB_s (a) and P-laden MB_s (b)

3.3 Phosphorus species of MB_s before and after adsorption

The NaOH-EDTA extracted 59.5–66.0% of the TP from the MB_s before and after P adsorption, with similar P species extracted. The results of the ^{31}P -NMR spectroscopy analysis showed that MB_s contained only orthophosphate and pyrophosphate before adsorption, while novel peaks of orthophosphate monoesters (5.0–4.3 ppm) and DNA (~0.7 ppm) were observed in the MB_s after adsorption (Table 3, Fig. 7) (Liu et al. 2018), indicating that solutions from livestock and poultry farms contain orthophosphate monoesters and DNA. Pyrophosphate has been reported to be directly involved in microbial activities and have a significant impact on P cycling (Xie et al. 2019). Furthermore, orthophosphate was the dominant P species in MB_s both before and after adsorption, ranging from 0.30–1.37 mg g^{-1} in MB_s and 7.99–9.44 mg g^{-1} in P-laden MB_s . Orthophosphate is the major P species directly available for plant uptake (Nash et al. 2014), which suggests that MB_s possess great potential as soil fertilizer to facilitate P resource recycling.

3.4 Phosphorus release from P-laden MB_s

The desorption kinetics of the P-laden MB_s revealed a slow release of P and the release rate gradually decreased within 192 h (Additional file 1: Fig S2). This might be attributed to the high concentration of P in the solution, where P release and adsorption approached a dynamic equilibrium. The data showed a good fit with the second-order kinetic model, with R^2 values of 0.98, 0.96, and 0.97 for MB-A_p , MB-C_p , and MB-T_p , respectively. The P release capacities of MB-A_p , MB-C_p , and MB-T_p were 8.24, 9.61, and 7.27 mg L^{-1} , respectively. In three consecutive cyclic release experiments, the amount of P released in each cycle was approximately consistent, indicating

the potential slow-release capability of the P-laden MB_s (An et al. 2021). Given that the P released into the soil by P-laden MB_s is promptly absorbed by plants, possibly intensifying the further release of P at soil–water interfaces (Yao et al. 2013), the slow release of P will contribute to reduce P loss and enhance P bioavailability for plants (Wang et al. 2021a, 2021b). The release patterns of the three treatments were consistent, with MB-C_p exhibiting the best P release capability.

3.5 Environmental implication

In this study, MB_s with stronger P adsorption capacities and magnetism were prepared from three types of emergent plant residues, enhancing P adsorb and enabling efficient recovery using magnets. The ^{31}P -NMR results showed that orthophosphate accounted for the largest proportion of the P constituents in the P-laden MB_s and is considered an ideal P fertilizer. Developing sustainable fertilizer as an alternative to conventional P fertilizer will promote environmentally friendly P supply and plant uptake efficiency. We anticipate that MB_s -based adsorbent will facilitate the reuse of P in additional scenarios, which are also under investigation by our research group.

4 Conclusions

In this study, we provide a novel approach for utilizing emergent plant residues from ecological ditches as P-adsorption materials. By successfully loading Fe compounds onto the surface of the three biochars, as validated by adsorption kinetics, MB-C was observed to have the best P adsorption capacity. Combined with the SEM-EDS, XRD, FTIR, and XPS characterization data analysis, inner-sphere complexation and electrostatic attraction were confirmed to play major roles in controlling P adsorption by the MB_s . The P species adsorbed by

the MB_s was mainly orthophosphate, proving the potential of the MB_s as carbon-based P fertilizer. Overall, this study provides an innovative idea for utilizing emergent plant residues as sustainable P resources, as well as proposes a feasible and eco-friendly scheme to reduce P pollution and promote P recycling in agricultural.

Supplementary Information

The online version contains supplementary material available at <https://doi.org/10.1007/s42773-024-00300-x>.

Additional file 1: Fig.S1. Magnetic biochar dispersed (a) and gathered under the power of magnets (b). **Fig.S2.** (a) The kinetic release of P from P-laden MB_s, (b) The cyclical P release of P-laden MB_s at 72 hours.

Acknowledgements

We acknowledge the Key Research and Development Project of Science and Technology Department of Zhejiang Province (2023C02016; 2023C02019), the National Key Research and Development Program of China (2022YFD1700704-3), the Bingtuan Science and Technology Program (2021DB019), and the Key Laboratory of Environment Remediation and Ecological Health, Ministry of Education, College of Environmental and Resource Sciences, Zhejiang University.

Author contributions

All authors contributed to the study conception and design. Material preparation, data collection and analysis were performed by HX, JY, YL, HX, HW, KME, XZ, CL, YF, YY and XL. The first draft of the manuscript was written by HX and all authors commented on previous versions of the manuscript. All authors read and approved the final manuscript.

Funding

This study was funded by the Key Research and Development Project of Science and Technology Department of Zhejiang Province (2023C02016; 2023C02019), the National Key Research and Development Program of China (2022YFD1700704-3), and Bingtuan Science and Technology Program (2021DB019).

Data availability

The datasets used or analyzed during the current study are available from the corresponding author on reasonable request.

Declarations

Competing interests

The authors have no relevant financial or non-financial interests to disclose.

Author details

¹Key Laboratory of Watershed Non-Point Source Pollution Control and Water Eco-Security of Ministry of Water Resources, College of Environmental and Resources Sciences, Zhejiang University, Hangzhou 310058, China. ²Department of Water Relations & Field Irrigation, National Research Centre, Cairo, Dokki 12622, Egypt. ³Key Laboratory of Mollisols Agroecology, Northeast Institute of Geography and Agroecology, Chinese Academy of Sciences, Harbin 150081, China. ⁴Australian Rivers Institute, School of Environment and Science, Griffith University, Nathan Campus, Brisbane QLD 4111, Australia. ⁵Sino-Japan Friendship Centre for Environmental Protection, Beijing 100029, China.

Received: 5 September 2023 Revised: 29 December 2023 Accepted: 3 January 2024

Published online: 26 February 2024

References

- Ahmad M, Rajapaksha AU, Lim JE, Zhang M, Bolan N, Mohan D, Vithanage M, Lee SS, Ok YS (2014) Biochar as a sorbent for contaminant management in soil and water: a review. *Chemosphere* 99:19–33. <https://doi.org/10.1016/j.jclepro.2018.11.087>
- Ai D, Ma H, Meng Y, Wei T, Wang B (2023) Phosphorus recovery and reuse in water bodies with simple ball-milled Ca-loaded biochar. *Sci Total Environ* 860:160502. <https://doi.org/10.1016/j.scitotenv.2022.160502>
- Ajmal Z, Muhmood A, Usman M, Kizito S, Lu JX, Dong RJ, Wu SB (2018) Phosphate removal from aqueous solution using iron oxides: adsorption, desorption and regeneration characteristics. *J Colloid Interface Sci* 528:145–155. <https://doi.org/10.1016/j.jcis.2018.05.084>
- An X, Wu Z, Yu J, Cravotto G, Liu X, Li Q, Yu B (2020) Coprolysis of biomass, bentonite, and nutrients as a new strategy for the synthesis of improved biochar-based slow-release fertilizers. *ACS Sustain Chem Eng* 8(8):3181–3190. <https://doi.org/10.1021/acssuschemeng.9b06483>
- Cade-Menun BJ, Preston CM (1996) A comparison of soil extraction procedures for 31 P NMR spectroscopy. *Soil Sci* 161:770–785. <https://doi.org/10.1080/00103620600710116>
- Chen H, Gao Y, Li J, Fang Z, Bolan N, Bhatnagar A, Gao B, Hou D, Wang S, Song H, Yang X, Shaheen SM, Meng J, Chen W, Rinklebe J, Wang H (2022) Engineered biochar for environmental decontamination in aquatic and soil systems: a review. *Carbon Res*. <https://doi.org/10.1007/s44246-022-00005-5>
- Cheng H, Yang S, Bolan N (2023) Biochar for future and futuristic biochar. *Pedosphere* 33:680–682. <https://doi.org/10.1016/j.pedsph.2023.07.023>
- Christopher C (2013) Emergent macrophyte biomass production. *Methods Biogeochem Wetlands* 10:137–153. <https://doi.org/10.2136/sssabookse110.c9>
- Conley DJ, Paerl HW, Howarth RW, Boesch DF, Seitzinger SP, Havens KE, Lancelot C, Likens GE (2009) Controlling eutrophication: nitrogen and phosphorus. *Science* 323:1014–1015. <https://doi.org/10.1126/science.1167755>
- Dai J, Meng X, Zhang Y, Huang Y (2020) Effects of modification and magnetization of rice straw derived biochar on adsorption of tetracycline from water. *Bioresour Technol* 311:123455. <https://doi.org/10.1016/j.biortech.2020.123455>
- Dong X, He L, Hu H, Liu N, Gao S, Piao Y (2018) Removal of 17β-estradiol by using highly adsorptive magnetic biochar nanoparticles from aqueous solution. *Chem Eng J* 352:371–379. <https://doi.org/10.1016/j.cej.2018.07.025>
- Drenkova-Tuhtan A, Mandel K, Paulus A, Meyer C, Hutter F, Gellermann C, Sextl G, Franzreb M, Steinmetz H (2013) Phosphate recovery from wastewater using engineered superparamagnetic particles modified with layered double hydroxide ion exchangers. *Water Res* 47:5670–5677. <https://doi.org/10.1016/j.watres.2013.06.039>
- Fang Y, Ali A, Gao Y, Zhao P, Li R, Li X, Liu J, Luo Y, Peng Y, Wang H, Liu H, Zhang Z, Pan J (2022) Preparation and characterization of MgO hybrid biochar and its mechanism for high efficient recovery of phosphorus from aqueous media. *Biochar* 4:40. <https://doi.org/10.1007/S42773-022-00171-0>
- Gao R, Fu Q, Hu H, Wang Q, Liu Y, Zhu J (2019) Highly-effective removal of pb by co-pyrolysis biochar derived from rape straw and orthophosphate. *J Hazard Mater* 371:191–197. <https://doi.org/10.1016/j.jhazmat.2019.02.079>
- Gong H, Tan Z, Zhang L, Huang Q (2019) Preparation of biochar with high absorbability and its nutrient adsorption–desorption behaviour. *Sci Total Environ* 694:133728. <https://doi.org/10.1016/j.scitotenv.2019.133728>
- Gusain R, Pandey B, Suthar S (2018) Composting as a sustainable option for managing biomass of aquatic weed *Pistia*: a biological hazard to aquatic system. *J Clean Prod* 177:803–812. <https://doi.org/10.1016/j.jclepro.2017.12.261>
- Hao S, Li Q, Qu J, An F, Zhang Y, Yu Z (2018) Neuron-inspired Fe₃O₄/conductive carbon filament network for high-speed and stable lithium storage. *ACS Appl Mater Inter* 10:17923–17932. <https://doi.org/10.1021/acsaami.8b03174>
- Hartley AM, House WA, Callow ME, Leadbeater BSC (1997) Coprecipitation of phosphate with calcite in the presence of photosynthesizing green algae. *Water Res*. [https://doi.org/10.1016/S0043-1354\(97\)00103-6](https://doi.org/10.1016/S0043-1354(97)00103-6)

- Huang Q, Song S, Chen Z, Hu B, Chen J, Wang X (2019) Biochar-based materials and their applications in removal of organic contaminants from wastewater: state-of-the-art review. *Biochar* 1:45–73. <https://doi.org/10.1007/s42773-019-00006-5>
- Huang H, Guo T, Wang K, Li Y, Zhang G (2021) Efficient activation of persulfate by a magnetic recyclable rape straw biochar catalyst for the degradation of tetracycline hydrochloride in water. *Sci Total Environ* 758:143957. <https://doi.org/10.1016/j.scitotenv.2020.143957>
- Iamchaturapatr J, Yi SW, Rhee JS (2007) Nutrient removals by 21 aquatic plants for vertical free surface-flow (VFS) constructed wetland. *Ecol Eng* 29:287–293. <https://doi.org/10.1016/j.ecoleng.2006.09.010>
- Jiang D, Chu B, Amano Y, Machida M (2018) Removal and recovery of phosphate from water by Mg-laden biochar: batch and column studies. *Colloids Surf, A* 558:429–437. <https://doi.org/10.1016/j.colsurfa.2018.09.016>
- Jiang Z, Yan L, Wu J, Liu X, Zhang J, Zheng Y, Pei Y (2020) Low-temperature synthesis of carbonate-intercalated Ni_xFe-layered double hydroxides for enhanced adsorption properties. *Appl Surf Sci* 531:147281. <https://doi.org/10.1016/j.apsusc.2020.147281>
- Klinar D (2016) Universal model of slow pyrolysis technology producing biochar and heat from standard biomass needed for the techno-economic assessment. *Bioresource Technol* 206:112–120. <https://doi.org/10.1016/j.biortech.2016.01.053>
- Kröger R, Moore MT (2011) Phosphorus dynamics within agricultural drainage ditches in the lower Mississippi Alluvial Valley. *Ecol Eng* 37:1905–1909. <https://doi.org/10.1016/j.ecoleng.2011.06.042>
- Kumwimba MN, Zhu B, Muyembe DK (2017) Assessing the influence of different plant species in drainage ditches on mitigation of non-point source pollutants (N, P, and sediments) in the Purple Sichuan Basin. *Environ Monit Assess* 189:1–14. <https://doi.org/10.1007/s10661-017-5965-8>
- Lei J, Lin J, Zhan Y, Zhang Z, Ma J (2021) Effectiveness and mechanism of aluminum/iron co-modified calcite capping and amendment for controlling phosphorus release from sediments. *J Environ Manage* 298:113471. <https://doi.org/10.1016/j.jenvman.2021.113471>
- Li R, Wang JJ, Zhou B, Awasthi MK, Ali A, Zhang Z, Lahori AH, Mahar A (2016) Recovery of phosphate from aqueous solution by magnesium oxide decorated magnetic biochar and its potential as phosphate-based fertilizer substitute. *Bioresource Technol* 215:209–214. <https://doi.org/10.1016/j.biortech.2016.02.125>
- Li J, Li B, Huang H, Lv X, Zhao N, Guo G, Zhang D (2019) Removal of phosphate from aqueous solution by dolomite-modified biochar derived from urban dewatered sewage sludge. *Sci Total Environ* 687:460–469. <https://doi.org/10.1016/j.scitotenv.2019.05.400>
- Liu J, Cade-Menun BJ, Yang J, Hu Y, Liu CW, Tremblay J, LaForge K, Schellenberg M, Hamel C, Bainard LD (2018) Long-term land use affects phosphorus speciation and the composition of phosphorus cycling genes in agricultural soils. *Front Microbiol* 9:1643. <https://doi.org/10.3389/fmicb.2018.01643>
- Liu X, Fu J, Tang Y, Smith RL Jr, Qi X (2021) Mg-coordinated self-assembly of MgO-doped ordered mesoporous carbons for selective recovery of phosphorus from aqueous solutions. *Chem Eng J* 406:126748. <https://doi.org/10.1016/j.cej.2020.126748>
- Liu M, Li R, Wang J, Liu X, Li S, Shen W (2022) Recovery of phosphate from aqueous solution by dewatered dry sludge biochar and its feasibility in fertilizer use. *Sci Total Environ* 814:152752. <https://doi.org/10.1016/j.scitotenv.2021.152752>
- Loganathan P, Vigneswaran S, Kandasamy J, Bolan NS (2014) Removal and recovery of phosphate from water using sorption. *Crit Rev Env Sci Tec* 44:847–907. <https://doi.org/10.1080/10643389.2012.741311>
- Malash GF, El-Khaiary MI (2010) Piecewise linear regression: a statistical method for the analysis of experimental adsorption data by the intraparticle-diffusion models. *Chem Eng J* 163:256–263. <https://doi.org/10.1016/j.cej.2010.07.059>
- MEP (2002) Discharge standard of pollutants for municipal wastewater treatment plant (GB18918-2002). China Environment Press, Beijing
- Min L, Zhang ZS, Zhe L, Haitao W (2020) Removal of nitrogen and phosphorus pollutants from water by FeCl₃-impregnated biochar. *Ecol Eng* 149:105792. <https://doi.org/10.1016/j.ecoleng.2020.105792>
- Mitrogiannis D, Psychoyoy M, Koukouzas N, Tsoukalas N, Palles D, Kamitsos E, Pantazidis A, Oikonomou G, Baziotis I (2018) Phosphate recovery from real fresh urine by Ca(OH)₂ treated natural zeolite. *Chem Eng J* 347:618–630. <https://doi.org/10.1016/j.cej.2018.04.102>
- Nash DM, Haygarth PM, Turner BL, Condon LM, McDowell RW, Richardson AE, Watkins M, Heaven MW (2014) Using organic phosphorus to sustain pasture productivity: a perspective. *Geoderma* 221:11–19. <https://doi.org/10.1016/j.geoderma.2013.12.004>
- Ou W, Lan X, Guo J, Cai A, Liu P, Liu N, Liu Y, Lei Y (2023) Preparation of iron/calcium-modified biochar for phosphate removal from industrial wastewater. *J Clean Prod* 383:135468. <https://doi.org/10.1016/j.jclepro.2022.135468>
- Padilla J, Watts D, Novak J, Cerven V, Ippolito J, Szogi A, Johnson M (2023) Magnesium activation affects the properties and phosphate sorption capacity of poultry litter biochar. *Biochar* 5:64. <https://doi.org/10.1007/s42773-023-00263-5>
- Palansooriya KN, Kim S, Igalavithana AD, Hashimoto Y, Choi Y, Mukhopadhyay R, Sarkar B, Ok YS (2021) Fe(III) loaded chitosan-biochar composite fibers for the removal of phosphate from water. *J Hazard Mater* 415:125464. <https://doi.org/10.1016/j.jhazmat.2021.125464>
- Pitakteeratham N, Hafuka A, Satoh H, Watanabe Y (2013) High efficiency removal of phosphate from water by zirconium sulfate-surfactant micelle mesostructure immobilized on polymer matrix. *Water Res* 47:3583–3590. <https://doi.org/10.1016/j.watres.2013.04.006>
- Reguyal F, Sarmah A, Gao W (2017) Synthesis of magnetic biochar from pine sawdust via oxidative hydrolysis of FeCl₂ for the removal of sulfamethoxazole from aqueous solution. *J Hazard Mater* 321:868–878. <https://doi.org/10.1016/j.jhazmat.2016.10.006>
- Shan X, Zhao Y, Bo S, Yang L, Xiao Z, An Q, Zhai S (2021) Magnetic aminated lignin/CeO₂/Fe₃O₄ composites with tailored interfacial chemistry and affinity for selective phosphate removal. *Sci Total Environ* 796:148984. <https://doi.org/10.1016/j.scitotenv.2021.148984>
- Shepherd JG, Joseph S, Sohi SP, Heal KV (2017) Biochar and enhanced phosphate capture: mapping mechanisms to functional properties. *Chemosphere* 179:57–74. <https://doi.org/10.1016/j.chemosphere.2017.02.123>
- Singh J, Kumar P, Eid EM, Taher MA, El-Morsy MHE, Osman HEM, Al-Bakre DA, Kumar V (2023) Phytoremediation of nitrogen and phosphorus pollutants from glass industry effluent by using water hyacinth (*Eichhornia crassipes* (Mart.) Solms): application of RSM and ANN techniques for experimental optimization. *Environ Sci Pollut R* 30:20590–20600. <https://doi.org/10.1007/s11356-022-23601-9>
- Smit AL, Bindraban PS, Conijn JG, van der Meer HG (2009) Phosphorus in agriculture: global resources, trends and developments. *Plant Research International* Bv, Wageningen, p 282
- Tang X, Lei Y, Yu C, Wang C, Zhang P, Lu H (2023) Highly-efficient degradation of organic pollutants by oxalic acid modified sludge biochar: mechanism and pathways. *Chemosphere* 325:138409. <https://doi.org/10.1016/j.chemosphere.2023.138409>
- Tran HN, You S, Hosseini-Bandegharaei A, Chao H (2017) Mistakes and inconsistencies regarding adsorption of contaminants from aqueous solutions: a critical review. *Water Res* 120:88–116. <https://doi.org/10.1016/j.watres.2017.04.014>
- Tu Y, Peng Z, Huang J, Wu X, Kong L, Liang Z, Yang L, Lin Z (2020) Preparation and characterization of magnetic biochar nanocomposites via a modified solvothermal method and their use as efficient heterogeneous Fenton-like catalysts. *Ind Eng Chem Res* 59:1809–1821. <https://doi.org/10.1021/acs.iecr.9b04590>
- Villanueva ME, Salinas A, Copello GJ, Díaz LE (2014) Point of zero charge as a factor to control biofilm formation of *Pseudomonas aeruginosa* in sol-gel derivatized aluminum alloy plates. *Surf Coat Technol* 254:145–150. <https://doi.org/10.1016/j.surfcoat.2014.05.074>
- Wang H, Xiao K, Yang J, Yu Z, Yu W, Xu Q, Wu Q, Liang S, Hu J, Hou H, Liu B (2020a) Phosphorus recovery from the liquid phase of anaerobic digesterate using biochar derived from iron-rich sludge: a potential phosphorus fertilizer. *Water Res* 174:115629. <https://doi.org/10.1016/j.watres.2020.115629>
- Wang Z, Hong S, Wen J, Ma C, Tang L, Jiang H, Chen J, Li S, Shen X, Yuan T (2020b) Lewis acid-facilitated deep eutectic solvent (DES) pretreatment for producing high-purity and antioxidative lignin. *ACS Sustain Chem Eng* 8:1050–1057. <https://doi.org/10.1021/acssuschemeng.9b05846>
- Wang B, Hu X, Zhou D, Zhang H, Chen R, Guo W, Wang H, Zhang W, Hong Z, Lyu W (2021a) Highly selective and sustainable clean-up of phosphate from aqueous phase by eco-friendly lanthanum cross-linked polyvinyl alcohol/alginate/palygorskite composite hydrogel beads. *J Clean Prod* 298:126878. <https://doi.org/10.1016/j.jclepro.2021.126878>

- Wang Z, Chen L, Liu C, Jin Y, Li F, Khan S, Liang X (2021b) Reduced colloidal phosphorus loss potential and enhanced phosphorus availability by manure-derived biochar addition to paddy soils. *Geoderma* 402:115348. <https://doi.org/10.1016/j.geoderma.2021.115348>
- Wang J, Jiang Y, Xu M, Han C, Zhang L, Liu G (2023) Resin-based iron-manganese binary oxide for phosphate selective removal. *Environ Sci Pollut Res* 30(2):4642–4652. <https://doi.org/10.1007/s11356-022-22525-8>
- Wu B, Wan J, Zhang Y, Pan B, Lo IMC (2020) Selective phosphate removal from water and wastewater using sorption: process fundamentals and removal mechanisms. *Environ Sci Technol* 54:50–66. <https://doi.org/10.1021/acs.est.9b05569>
- Wu D, Shen C, Cheng Y, Ding J, Li W (2023) Phosphorus removal by aquatic vegetation in shallow eutrophic lakes: a laboratory study. *Environ Sci Pollut R* 30:16166–16177. <https://doi.org/10.1007/s11356-022-23403-z>
- Xie F, Wu F, Liu G, Mu Y, Feng C, Wang H, Giesy JP (2014) Removal of phosphate from eutrophic lakes through adsorption by in situ formation of magnesium hydroxide from diatomite. *Environ Sci Technol* 48:582–590. <https://doi.org/10.1021/es4037379>
- Xie F, Li L, Song K, Li G, Wu F, Giesy JP (2019) Characterization of phosphorus forms in a eutrophic lake, China. *Sci Total Environ* 659:1437–1447. <https://doi.org/10.1016/j.scitotenv.2018.12.466>
- Xu Q, Chen Z, Wu Z, Xu F, Yang D, He Q, Li G, Chen Y (2019) Novel lanthanum doped biochars derived from lignocellulosic wastes for efficient phosphate removal and regeneration. *Bioresour Technol* 289:121600. <https://doi.org/10.1016/j.biortech.2019.121600>
- Yamashita T, Hayes P (2008) Analysis of XPS spectra of Fe²⁺ and Fe³⁺ ions in oxide materials. *Appl Surf Sci* 254:2441–2449. <https://doi.org/10.1016/j.apsusc.2007.09.063>
- Yang Q, Wang X, Luo W, Sun J, Xu Q, Chen F, Zhao J, Wang S, Yao F, Wang D, Li X, Zeng G (2018) Effectiveness and mechanisms of phosphate adsorption on iron-modified biochars derived from waste activated sludge. *Bioresour Technol* 247:537–544. <https://doi.org/10.1016/j.biortech.2017.09.136>
- Yang J, Wang Z, Li R, Xu X, Liu J, Huang Y, Ye X, Wang W (2022) Effect of Fe (III) modification on the phosphorus removal behavior of Ce (III) carbonate adsorbents. *ACS Omega* 7(36):31767–31777. <https://doi.org/10.1021/acsomega.2c02269>
- Yao Y, Gao B, Chen J, Yang L (2013) Engineered biochar reclaiming phosphate from aqueous solutions: Mechanisms and potential application as a slow-release fertilizer. *Environ Sci Technol* 47:8700–8708. <https://doi.org/10.1021/es4012977>
- Yi Y, Tu G, Zhao D, Tsang P, Fang Z (2019) Biomass waste components significantly influence the removal of Cr(VI) using magnetic biochar derived from four types of feedstocks and steel pickling waste liquor. *Chem Eng J* 360:212–220. <https://doi.org/10.1016/j.cej.2018.11.205>
- Yin Q, Ren H, Wang R, Zhao Z (2018) Evaluation of nitrate and phosphate adsorption on Al-modified biochar: influence of Al content. *Sci Total Environ* 631:895–903. <https://doi.org/10.1016/j.scitotenv.2018.03.091>
- Yu C, Shi C, Ji M, Xu X, Zhang Z, Ma J, Wang G (2019) Taste and odor compounds associated with aquatic plants in Taihu lake: distribution and producing potential. *Environ Sci Pollut R* 26:34510–34520. <https://doi.org/10.1007/s11356-019-06188-6>
- Yu J, Feng H, Tang L, Pang Y, Wang J, Zou J, Xie Q, Liu Y, Feng C, Wang J (2021) Insight into the key factors in fast adsorption of organic pollutants by hierarchical porous biochar. *J Hazard Mater* 403:123610. <https://doi.org/10.1016/j.jhazmat.2020.123610>
- Zhang B, Wang L, Li Y (2019) Fractionation and identification of iron-phosphorus compounds in sewage sludge. *Chemosphere* 223:250–256. <https://doi.org/10.1016/j.chemosphere.2019.02.052>
- Zhao D, Qiu S, Li M, Luo Y, Zhang L, Feng M, Yuan M, Zhang K, Wang F (2022) Modified biochar improves the storage capacity and adsorption affinity of organic phosphorus in soil. *Environ Res* 205:112455. <https://doi.org/10.1016/j.envres.2021.112455>
- Zhou Z, Liu Y, Liu S, Liu H, Zeng G, Tan X, Yang C, Ding Y, Yan Z, Cai X (2017) Sorption performance and mechanisms of arsenic (V) removal by magnetic gelatin-modified biochar. *Chem Eng J* 314:223–231. <https://doi.org/10.1016/j.cej.2016.12.113>